

Spin Dynamics Formalism for ^{23}Na in Biological Tissue

Chengchuan Wu¹, Yasmin Blunck¹, Leigh A. Johnston¹

Department of Biomedical Engineering and Melbourne Brain Centre Imaging Unit, The University of Melbourne, Australia

Abstract

The dynamics of the ^{23}Na spin system in biological systems are encapsulated in an algebraic model based on the tensor operator basis, that for the first time provides a general specification of time-varying RF excitation, field inhomogeneities and relaxation. Using the proposed ‘Sodium Bloch equation’, simulations of three classical ^{23}Na pulse sequences are performed to demonstrate the versatility and applicability of the model, returning the evolution of the ^{23}Na spin system during these experiments: soft rectangular inversion, adiabatic inversion and triple-quantum filtering. The model is straightforward to implement as a single 15x15 system matrix and one-line call to an ode solver, providing a computationally efficient and accessible method for use in ^{23}Na pulse and pulse sequence design.

Keywords: Sodium NMR, ^{23}Na NMR, sodium MRI, spherical tensor operator basis

1. Introduction

The quadrupolar sodium nucleus is fundamental to numerous biological processes and is a sensitive biomarker of tissue viability and organ function abnormality [1]. The isotope ^{23}Na , with nearly 100% abundance, is the second largest NMR signal source in-vivo and offers great potential for non-proton imaging in basic and clinical research studies [1–3]. The Bloch equation (BE), fundamental to pulse and pulse sequence design in MRI, is an algebraic model of bulk magnetisation in biological tissue for spin-1/2 nuclei, parameterised by relaxation time constants, off-resonance and time-varying RF field. For ^{23}Na however, the spin system dynamics are far less accessible than the ^1H case, lacking a generalised algebraic formalism for describing the spin system behaviour in biological tissue.

In this work, we provide a framework for ^{23}Na spin dynamics in biological tissue, based on irreducible spherical tensor operator (ISTO) formalism. We demonstrate that the Redfield equation can be simplified in biological ^{23}Na magnetic resonance, and derive the framework we refer to (albeit somewhat facetiously) as the ‘Sodium Bloch equation’ (SBE), with obvious analogy to the spin-1/2 Bloch equation. Importantly, this framework explicitly models relaxation and off-resonance effects concurrently with arbitrary time-varying RF field, producing efficient and accurate numerical solutions.

The quantum state of the spin-3/2 ^{23}Na ensemble as represented by the density operator requires a 16-dimensional linear space for complete quantum mechanical description. Its dynamics are governed by the Liouville-von Neumann equation and complemented by the Redfield theory for secularised description of the relaxation process. These theories can be conveniently formulated in the ISTO basis in which the dependency on experimental parameters is addressed [4–7]. However, a framework for comprehensive description of the sodium spin dynamics in biological material has not previously been available due to the complexity of the Redfield equation; approaches in the literature present special cases in which the relaxation is absent or decoupled from other interactions. These approaches model selected ^{23}Na NMR experiments such as triple-quantum filtering (TQF) [7, 8], steady-state free precession [6] and soft inversion [9, 10].

For ^{23}Na spin dynamics under modulated RF fields, the spin-1/2 Bloch equation are commonly used as a first order approximation [11, 12]. The spin-1/2 Bloch equation accurately describes the ^{23}Na spin behaviour in fast-motion,

isotropic fluid in which the ^{23}Na spin dynamics reduce to the spin-1/2 case. However, in tissue where the molecular motion is slow and the electric field gradient (EFG) is anisotropic, the spin-1/2 Bloch equation fails to include the multiple-quantum coherences that produce bi-exponential decay and multiple-quantum filtered signals.

The properties of the SBE proposed here-in are expounded by the generation of three types of ^{23}Na MRI sequences: soft rectangular pulse inversion, adiabatic inversion and triple-quantum filtering sequences. This demonstrates the broad applicability of the proposed framework across a wide range of sodium pulse sequences, and provides insight into the deviation of the spin-3/2 system dynamics from their spin-1/2 counterpart.

2. Theory of ^{23}Na spin dynamics in biological systems

In this work, all physical quantities are described in the RF rotating frame. The dynamics of the density operator $\hat{\rho}$ can be described by the master equation incorporating the Redfield relaxation function $\hat{\Gamma}$ [13, 14],

$$\frac{d}{dt}\hat{\rho}(t) = -i[\hat{H}_D, \hat{\rho}(t)] - \hat{\Gamma}(\hat{\rho}(t) - \hat{\rho}_0), \quad (1)$$

where $\hat{\rho}_0$ denotes the density operator at thermal equilibrium and \hat{H}_D denotes the Hamiltonian of deterministic propagation consisting of three terms,

$$\hat{H}_D = \hat{H}_\Delta + \hat{H}_1 + \hat{H}_{QS}. \quad (2)$$

Here, \hat{H}_Δ , \hat{H}_1 and \hat{H}_{QS} derive from the effective static magnetic field, the RF field and the time-averaged quadrupolar EFG, respectively.

The relaxation superoperator describes the interaction with the fluctuating quadrupolar Hamiltonian \hat{H}_{QF} [5, 7, 13],

$$\hat{\Gamma}(\hat{\rho}(t) - \hat{\rho}_0) = \int_0^\infty [\hat{H}_{QF}(t), [\exp\{-i\hat{H}_D\tau\} \hat{H}_{QF}(t-\tau) \exp\{i\hat{H}_D\tau\}, \hat{\rho}(t) - \hat{\rho}_0]] d\tau. \quad (3)$$

Due to the linear properties of the spin system, the commutation and the relaxation superoperator acting on $\hat{\rho}$ can be represented as matrices **D** and **R** applied to **P**, the vector representation of $\hat{\rho}$. The equilibrium-state, $\hat{\rho}_0$, gives rise to an offset term, **C**. Therefore Eq.1 can be written in a form akin to the Bloch equation, as

$$\begin{aligned} \frac{d}{dt}\mathbf{P} &= (\mathbf{D} + \mathbf{R})\mathbf{P} + \mathbf{C} \\ &= \mathbf{L}\mathbf{P} + \mathbf{C}. \end{aligned} \quad (4)$$

Here, **L** is the 15x15 system matrix of the SBE. Fig.1 details the entries of **L**, colour-coded for intuitive understanding of the origins of the terms, as outlined in the following sections. The matrix **L** is parameterised by RF amplitude (nutation frequency), $\omega_1(t)$, the initial RF phase, ϕ_0 with reference to the x'-axis, off-resonance frequency, $\omega_\Delta(t)$, time-average residual quadrupolar frequency, ω_Q , and spectral densities, J_0 , J_1 and J_2 .

To derive the system matrix **L** and offset **C**, we express the density operator and Hamiltonians in terms of the ISTO basis consisting of orthonormal components,

$$\{\hat{T}_{l0}, \hat{T}_{lm}(a), \hat{T}_{lm}(s) \mid l = 0, 1, 2, 3, m = 1, \dots, l\}, \quad (5)$$

where l and m are the rank and coherence order of the tensor operator, respectively [1]. Under this treatment, $\hat{T}_{11}(a)$, $\hat{T}_{11}(s)$ and \hat{T}_{10} are proportional to the x-, y- and z-angular momentum operators, respectively, while T_{00} is the identity operator. Given the assumption that the spin ensemble is isolated, T_{00} has no contribution to the spin dynamics and therefore can be omitted [5], forming the reduced basis,

$$\{\hat{T}_{10}, \hat{T}_{11}(a), \hat{T}_{11}(s), \hat{T}_{20}, \hat{T}_{21}(a), \hat{T}_{21}(s), \hat{T}_{22}(a), \hat{T}_{22}(s), \hat{T}_{30}, \hat{T}_{31}(a), \hat{T}_{31}(s), \hat{T}_{32}(a), \hat{T}_{32}(s), \hat{T}_{33}(a), \hat{T}_{33}(s)\}. \quad (6)$$

$-\frac{2j_1}{5} - \frac{8j_2}{5}$	$-\omega_1(t) \sin \phi_0$	$-i\omega_1(t) \cos \phi_0$	0	0	0	0	$-\frac{4j_1}{5} + \frac{4j_2}{5}$	0	0	0	0	0	0			
$\omega_1(t) \sin \phi_0$	$-\frac{3j_0}{5} - j_1 - \frac{2j_2}{5}$	$i\omega_\Delta(t)$	0	0	$i\sqrt{3/5}\omega_Q$	0	0	$-\frac{\sqrt{6}j_0}{5} + \frac{\sqrt{6}j_2}{5}$	0	0	0	0	0			
$-i\omega_1(t) \cos \phi_0$	$i\omega_\Delta(t)$	$-\frac{3j_0}{5} - j_1 - \frac{2j_2}{5}$	0	$i\sqrt{3/5}\omega_Q$	0	0	0	$-\frac{\sqrt{6}j_0}{5} + \frac{\sqrt{6}j_2}{5}$	0	0	0	0	0			
0	0	0	$-2j_1 - 2j_2$	$-\sqrt{3}\omega_1(t) \sin \phi_0 - i\sqrt{3}\omega_1(t) \cos \phi_0$	0	0	0	0	0	0	0	0	0			
0	0	$i\sqrt{3/5}\omega_Q$	$\sqrt{3}\omega_1(t) \sin \phi_0$	$-j_0 - j_1 - 2j_2$	$i\omega_\Delta(t)$	$-i\omega_1(t) \cos \phi_0 - \omega_1(t) \sin \phi_0$	0	0	$i\sqrt{2/5}\omega_Q$	0	0	0	0	0		
0	$i\sqrt{3/5}\omega_Q$	0	$-i\sqrt{3}\omega_1(t) \cos \phi_0$	$i\omega_\Delta(t)$	$-j_0 - j_1 - 2j_2$	$-\omega_1(t) \sin \phi_0 - i\omega_1(t) \cos \phi_0$	0	$i\sqrt{2/5}\omega_Q$	0	0	0	0	0	0		
0	0	0	0	$-i\omega_1(t) \cos \phi_0$	$\omega_1(t) \sin \phi_0$	$-j_0 - 2j_1 - j_2$	$i2\omega_\Delta(t)$	0	0	0	$i\omega_Q$	0	0	0		
0	0	0	0	$\omega_1(t) \sin \phi_0$	$-i\omega_1(t) \cos \phi_0$	$i2\omega_\Delta(t)$	$-j_0 - 2j_1 - j_2$	0	0	$i\omega_Q$	0	0	0	0		
$-\frac{4j_1}{5} + \frac{4j_2}{5}$	0	0	0	0	0	0	$-\frac{8j_1}{5} - \frac{2j_2}{5}$	$-\sqrt{6}\omega_1(t) \sin \phi_0 - i\sqrt{6}\omega_1(t) \cos \phi_0$	0	0	0	0	0			
0	$-\frac{\sqrt{6}j_0}{5} + \frac{\sqrt{6}j_2}{5}$	0	0	0	$i\sqrt{2/5}\omega_Q$	0	0	$\sqrt{6}\omega_1(t) \sin \phi_0$	$-\frac{2j_0}{5} - j_1 - \frac{3j_2}{5}$	$i\omega_\Delta(t)$	$-i\sqrt{\frac{5}{2}}\omega_1(t) \cos \phi_0 - \sqrt{\frac{5}{2}}\omega_1(t) \sin \phi_0$	0	0	0		
0	$-\frac{\sqrt{6}j_0}{5} + \frac{\sqrt{6}j_2}{5}$	0	$i\sqrt{2/5}\omega_Q$	0	0	0	$-i\sqrt{6}\omega_1(t) \cos \phi_0$	$i\omega_\Delta(t)$	$-\frac{2j_0}{5} - j_1 - \frac{3j_2}{5}$	$-\sqrt{\frac{5}{2}}\omega_1(t) \sin \phi_0 - i\sqrt{\frac{5}{2}}\omega_1(t) \cos \phi_0$	0	0	0	0		
0	0	0	0	0	0	$i\omega_Q$	0	0	$-i\sqrt{\frac{5}{2}}\omega_1(t) \cos \phi_0$	$\frac{5}{2}\omega_1(t) \sin \phi_0$	$-j_0 - j_2$	$i2\omega_\Delta(t)$	$-i\sqrt{\frac{3}{2}}\omega_1(t) \cos \phi_0 - \sqrt{\frac{3}{2}}\omega_1(t) \sin \phi_0$	0	0	0
0	0	0	0	0	0	$i\omega_Q$	0	0	$\sqrt{\frac{5}{2}}\omega_1(t) \sin \phi_0 - i\sqrt{\frac{5}{2}}\omega_1(t) \cos \phi_0$	$i2\omega_\Delta(t)$	$-j_0 - j_2$	$-i\sqrt{\frac{3}{2}}\omega_1(t) \sin \phi_0 - i\sqrt{\frac{3}{2}}\omega_1(t) \cos \phi_0$	0	0	0	
0	0	0	0	0	0	0	0	0	0	$-i\sqrt{\frac{3}{2}}\omega_1(t) \cos \phi_0$	$\sqrt{\frac{3}{2}}\omega_1(t) \sin \phi_0$	$-j_1 - j_2$	$i3\omega_\Delta(t)$	0	0	0
0	0	0	0	0	0	0	0	0	0	$\sqrt{\frac{3}{2}}\omega_1(t) \sin \phi_0 - i\sqrt{\frac{3}{2}}\omega_1(t) \cos \phi_0$	$i3\omega_\Delta(t)$	$-j_1 - j_2$	0	0	0	0

Figure 1: The Sodium Bloch Equation system matrix, \mathbf{L} , colour-coded to indicate source of terms: Red-shaded entries are associated with RF excitation; Yellow-shaded entries are off-resonance terms; Green-shaded terms are associated with residual quadrupolar oscillation; Blue-shaded terms are associated with the fluctuating quadrupolar interaction. (color should be used for this figure in print)

Note that we use two forms of ISTO bases interchangeably; the relationship between the native ISTOs, $\{\hat{T}_{lm} \mid l = 1, 2, 3, m = -l, \dots, l\}$, and the symmetric (s) and antisymmetric (a) ISTOs is given by [5]:

$$\hat{T}_{lm}(s) = \frac{1}{\sqrt{2}} (\hat{T}_{l-m} + \hat{T}_{lm}) \quad (7a)$$

$$\hat{T}_{lm}(a) = \frac{1}{\sqrt{2}} (\hat{T}_{l-m} - \hat{T}_{lm}). \quad (7b)$$

2.1. The Deterministic Matrix \mathbf{D}

The generator, \mathbf{D} , of the system matrix \mathbf{L} in (4) gives rise to deterministic spin dynamics, i.e. nutation, free precession and quadrupolar coupling. By definition, the commutator is

$$\begin{aligned} \mathbf{D} &\stackrel{\Delta}{=} -i[\hat{H}_D, \mathbf{E}] \\ &= -i \left[\sqrt{5}\omega_\Delta \hat{T}_{10} + \sqrt{5}\omega_1 e^{i\phi_0} \hat{T}_{11}(a) + \omega_Q \hat{T}_{20}, \mathbf{E} \right] \\ &= -i \left[\sqrt{5}\omega_\Delta \hat{T}_{10}, \mathbf{E} \right] - i \left[\sqrt{5}\omega_1 e^{i\phi_0} \hat{T}_{11}(a), \mathbf{E} \right] - i [\omega_Q \hat{T}_{20}, \mathbf{E}], \end{aligned} \quad (8)$$

where \mathbf{E} is the identity matrix and is equivalent to the sum of the ISTOs. The matrix form \mathbf{D} results from expanding the commutators using commutation laws [4, 5, 15].

The non-zero elements of \mathbf{D} are shaded yellow, red and green in Fig. 1, corresponding to off-resonance precession, nutation and static quadrupolar coupling, respectively.

2.2. The Relaxation Matrix \mathbf{R}

With \hat{H}_{QF} expressed in the tensor operator basis, the relaxation superoperator has the form [8]

$$\hat{\Gamma}(\hat{\rho}) = - \int_0^\infty \sum_{m=-2}^2 \left[\hat{T}_{2m}, \left[e^{-i\hat{H}_D\tau} \hat{T}_{2m}^\dagger e^{i\hat{H}_D\tau}, \hat{\rho} \right] \right] \left(\frac{eQ}{\hbar} \right)^2 \langle [F_{2m}^*(t) - \langle F_{2m}^* \rangle] [F_{2m}(t-\tau) - \langle F_{2m} \rangle] \rangle e^{im\omega_r\tau} d\tau, \quad (9)$$

where $\hat{T}_{2m}^\dagger = (-1)^m \hat{T}_{2-m}$, e is the unit electric charge, Q is the quadrupole moment, F_{2m} is the EFG tensor component, ω_r is the frequency of the rotating frame, $\langle \cdot \rangle$ and $*$ denote motion average and complex conjugation, respectively.

The integral in Eq.9 cannot be resolved except in certain cases. If \hat{H}_D is absent, a matrix representation of \mathbf{R} results [5]. We demonstrate in the Appendix that \mathbf{R} has the same form (blue shaded entries in Fig. 1) given any practical \hat{H}_D for ^{23}Na NMR in biological tissue environments.

2.3. The Offset \mathbf{C}

If thermal equilibrium, $\hat{\rho}_0 = \mathbf{P}(0) = \hat{T}_{10}$, is assumed, the offset can be determined by applying the initial condition $\mathbf{C} = -\mathbf{R}\mathbf{P}(0)$, such that

$$\mathbf{C} = \left[\frac{2}{5}J_1 + \frac{8}{5}J_2, 0, 0, 0, 0, 0, 0, 0, \frac{4}{5}J_1 - \frac{4}{5}J_2, 0, 0, 0, 0, 0, 0 \right]^\top. \quad (10)$$

With these definitions of \mathbf{L} and \mathbf{C} , the SBE as defined by Eq. 4 is fully described.

3. Methods

Numerical integration is used to solve the Sodium Bloch equation in MATLAB (Mathworks, Natick, MA) using the Runge-Kutta method (*ode45*). The complete script is available at https://github.com/chengchuanw/Sodium_spin_dynamics_simulator.

Three types of motion regimes were chosen with measured spectral density values taken from [16]:

1. **50 mM saline (isotropic, fast-motion regime):** $J_0 = J_1 = J_2 = 8.9$ Hz, $\omega_Q = 0$ Hz;
2. **8% agar (isotropic, slow-motion regime):** $J_0 = 250$ Hz, $J_1 = 45.4$ Hz, $J_2 = 19.3$ Hz, $\omega_Q = 0$ Hz;
3. **3% xanthan (anisotropic, slow-motion regime):** $J_0 = 319$ Hz, $J_1 = 28.2$ Hz, $J_2 = 28.1$ Hz, $\omega_Q = 61.8$ Hz.

The time evolution of ^{23}Na in these motion regimes during three types of ^{23}Na pulse sequences were simulated. Each simulation took only a few seconds to finish on a standard laptop. For the first two sequences, simulations of the spin-1/2 Bloch equation were also performed for comparison. The proton relaxation parameters were approximated by the “apparent” T_1 and T_2 , defined as the times required for the longitudinal magnetisation to recover to 63% of its maximum from null, and for the transverse magnetisation to decay 37% from equilibrium. For 50 mM saline, $T_1 = 56.7$ ms, $T_2 = 56$ ms. For 8% agar, $T_1 = 21.7$ ms, $T_2 = 6.0$ ms, and for 3% xanthan, $T_1 = 17.3$ ms, $T_2 = 3.7$ ms.

Pulse Duration Effect on Magnetisation Inversion

To examine the combined effect of RF and relaxation, we simulated the time evolution of on-resonance ^{23}Na during 180° pulses, with the duration of the pulse stepped between 500 μ s, 1 ms, 5 ms and 10 ms.

Adiabatic Inversion Pulse

To examine the response of the ^{23}Na spin system to modulated pulses, we simulated the adiabatic Wide-band Uniform Rate and Smooth Truncation (WURST) inversion pulse sequence [11]. The amplitude of the pulse is modulated by

$$\omega_1(t) = 2\pi v_1 \left(1 - \left| \sin\left(\frac{\pi(2t - T_p)}{2T_p}\right) \right|^n \right), \quad (11)$$

where v_1 is the amplitude in Hz, the pulse duration T_p was chosen to be 10 ms and the factor n was chosen to be 20. The frequency of the pulse is given by

$$\phi(t) = \frac{\pi\Delta f}{T_p} t^2. \quad (12)$$

The frequency sweep range, Δf , was chosen to be 2 kHz.

Triple-Quantum Filtering

To examine multiple-quantum coherences, we simulated a six-step TQF experiment, following the three-pulse experiment setup in [17]. Hard pulses of $500 \mu\text{s}$ were employed. The first pulse was phase cycled through $30^\circ, 90^\circ, 150^\circ, -150^\circ, -90^\circ, -30^\circ$. After the preparation time of 3 ms , the second pulse was applied with a phase offset of 90° with reference to the first pulse. The third pulse followed after a $400 \mu\text{s}$ delay with phase of 0° . The final triple-quantum filtered result was obtained by summing the signals with their signs toggled between + and - in turn.

4. Results

Pulse Duration Effect on Magnetisation Inversion

Fig.2 shows the time evolution of the longitudinal magnetisation (\hat{T}_{10}) during inversion pulse with various pulse durations. The results from the Sodium Bloch equation agree well with the literature [10]. The comparison between the SBE and proton Bloch equation demonstrates negligible difference for saline, as expected. For agar and xanthan, differences can be found between the two spin system models, which increase with the duration of the pulse.

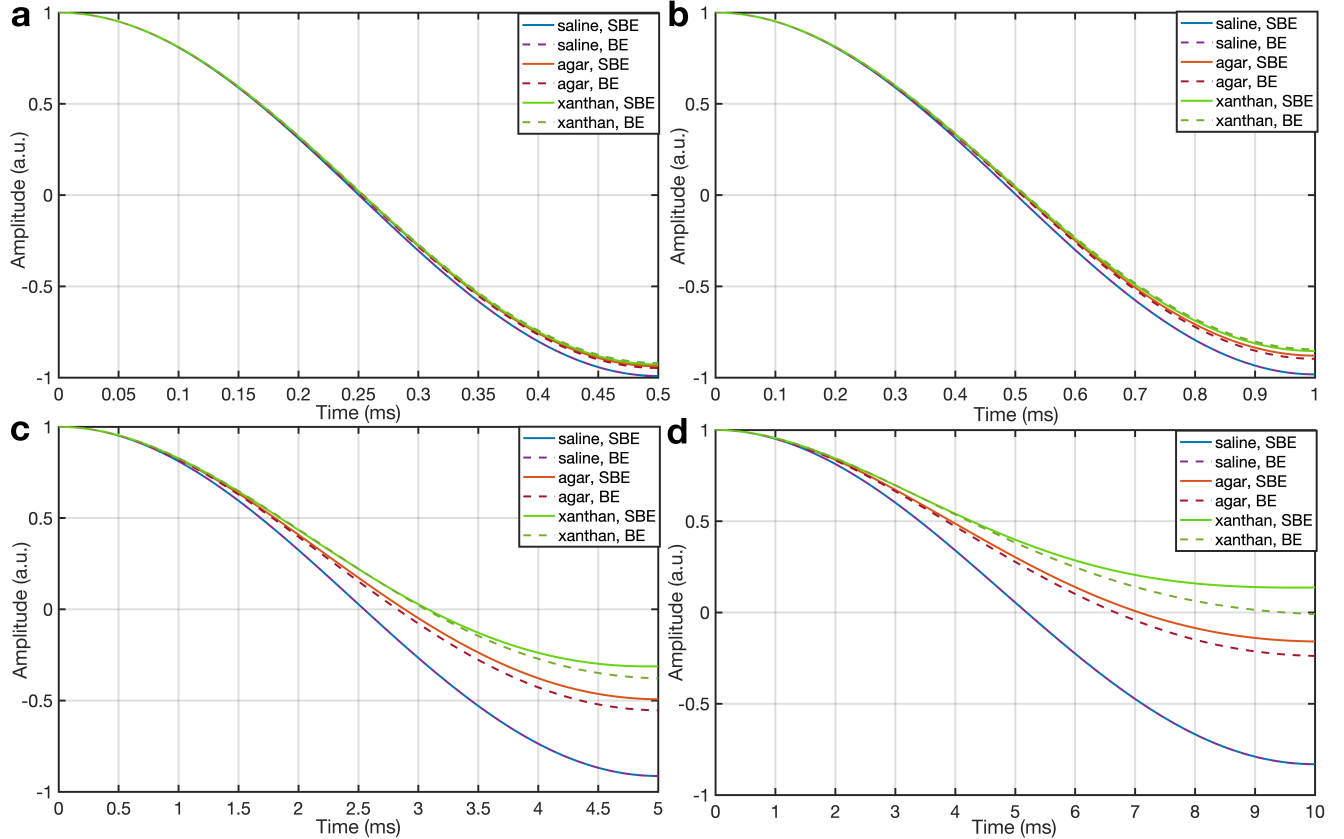


Figure 2: The effect of pulse duration and comparison of Sodium Bloch Equation and Bloch Equation. Evolution of the longitudinal magnetisation under inversion pulses with duration of (a) $500 \mu\text{s}$; (b) 1 ms ; (c) 5 ms ; (d) 10 ms . (color should be used for this figure in print)

Adiabatic Inversion Pulse

The pulse shape and the simulated magnetisation evolution are shown in Fig.3. Although the inversion pulse duration is 10 ms long, significant difference was not observed between SBE and BE, unlike the results for the 10 ms soft

pulse inversion in the previous simulation. Fig.4 shows that the proposed SBE can be used to evaluate the pulse sequence under off-resonance. Fig.4(a) depicts the longitudinal magnetisation evolution during the preparatory phase of the sequence, in the presence of off-resonances ranging from -50 to 50 Hz. The longitudinal magnetisation amplitude at the end of the preparatory phase is shown in Fig.4(b), which assesses robustness against B_0 inhomogeneity.

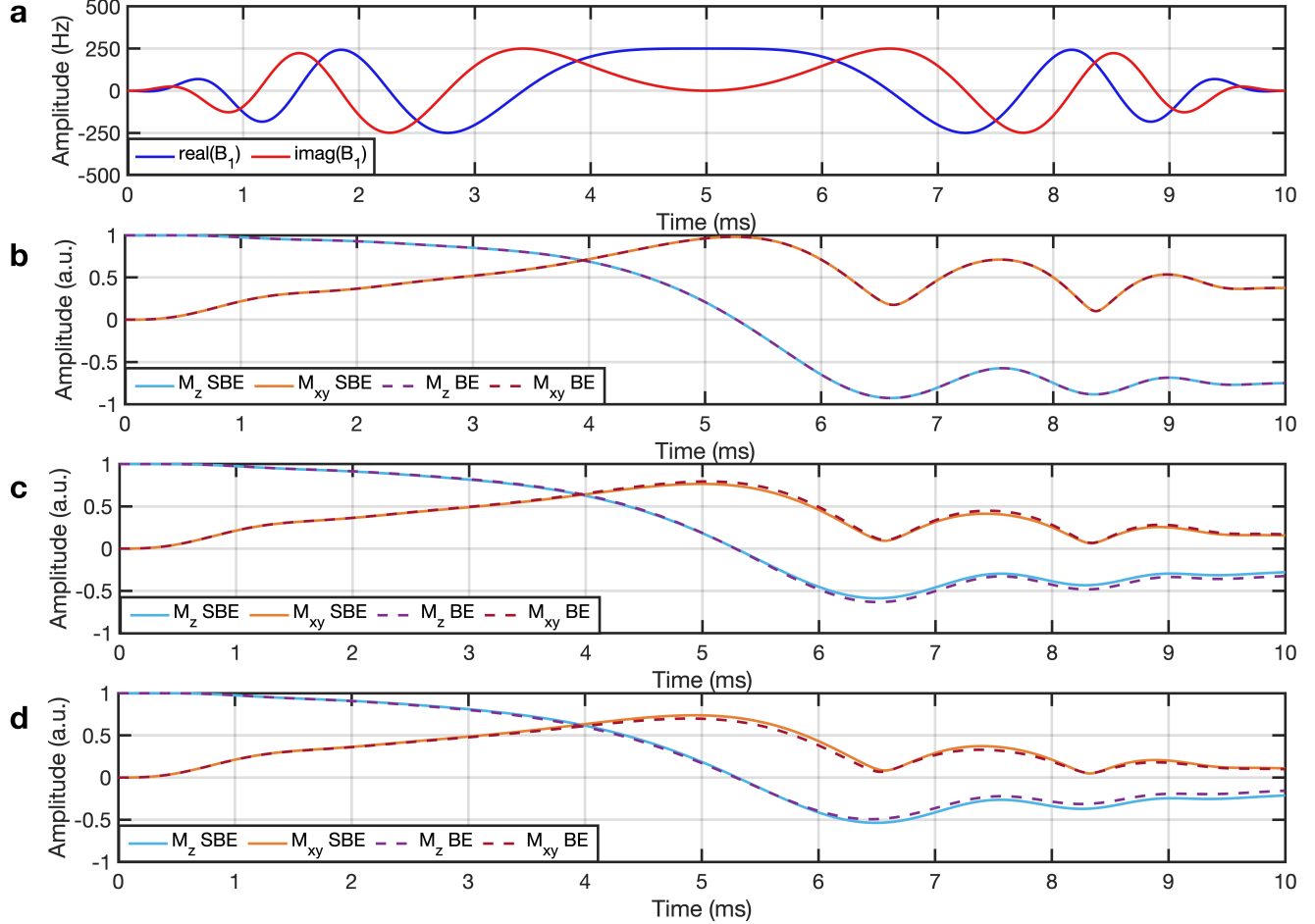


Figure 3: (a) Shape of the WURST inversion pulse, and the evolution of bulk magnetisation in (b) saline, (c) agar, (d) xanthan. (color should be used for this figure in print)

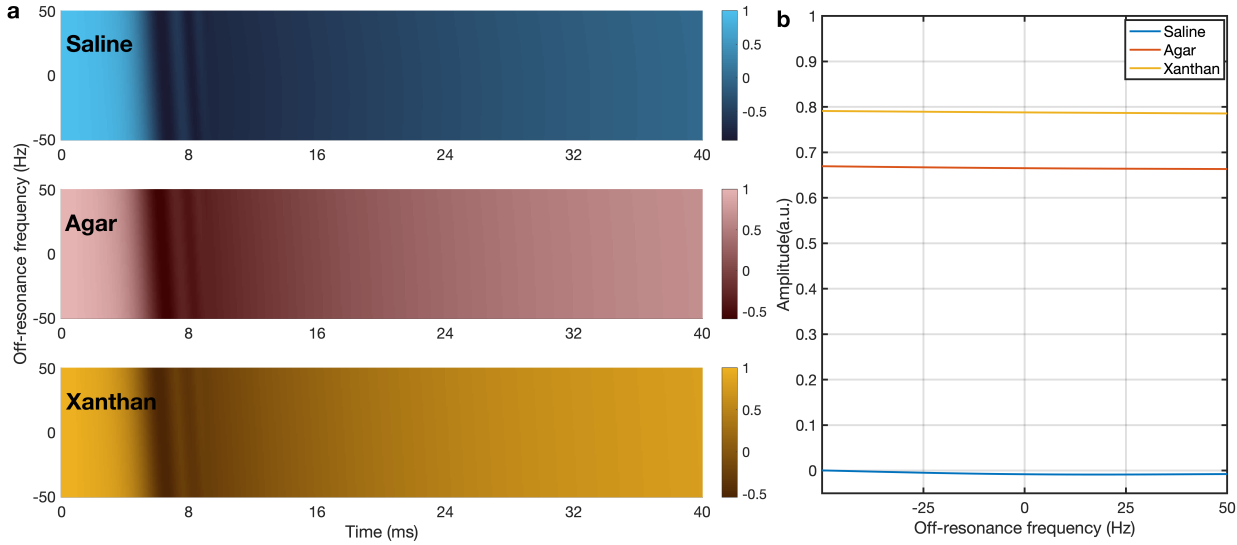


Figure 4: Sodium Bloch Equation simulation depicting the amplitude of the longitudinal magnetisation during the preparatory stage of the WURST IR pulse (a) with the influence of B_0 inhomogeneity, and (b) their values at the end of the preparatory stage. (color should be used for this figure in print)

Triple-quantum Filtering

Figs.5 and 6 display the components of different ranks and orders in each phase cycling step in the xanthan environment with reference to the detector phase. Fig.7 shows the sums over the phase cycling steps to exhibit the rise of the observable signal (the rank-1 order-1 component) transferred from the rank-3 order-3 component.

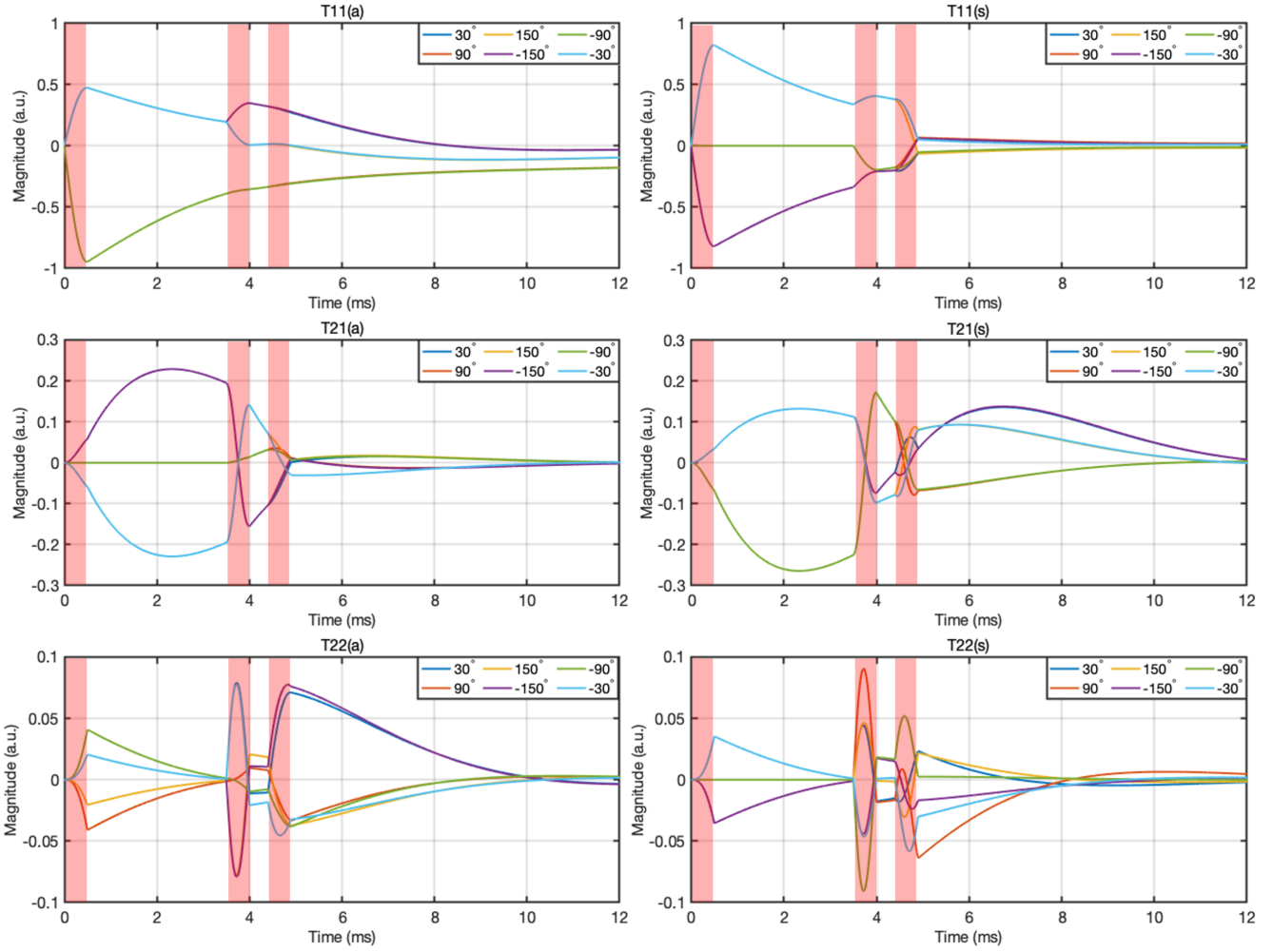


Figure 5: Evolution of the rank-1 and rank-2 coherences during the three-pulse TQF experiment. The red bars indicate periods of RF excitation. (color should be used for this figure in print)

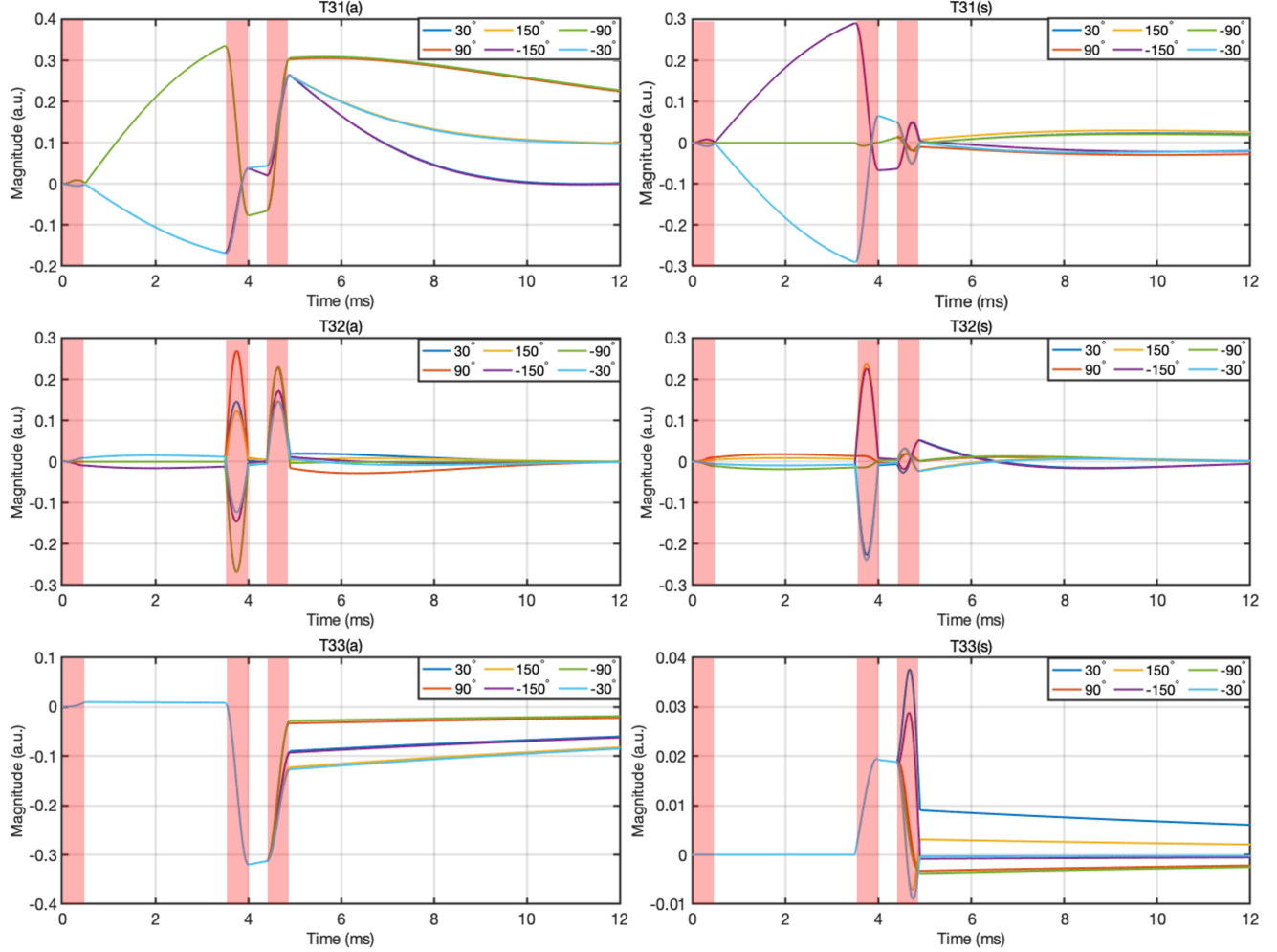


Figure 6: Evolution of the rank-3 coherences during the three-pulse TQF experiment. The red bars indicate periods of RF excitation. (color should be used for this figure in print)

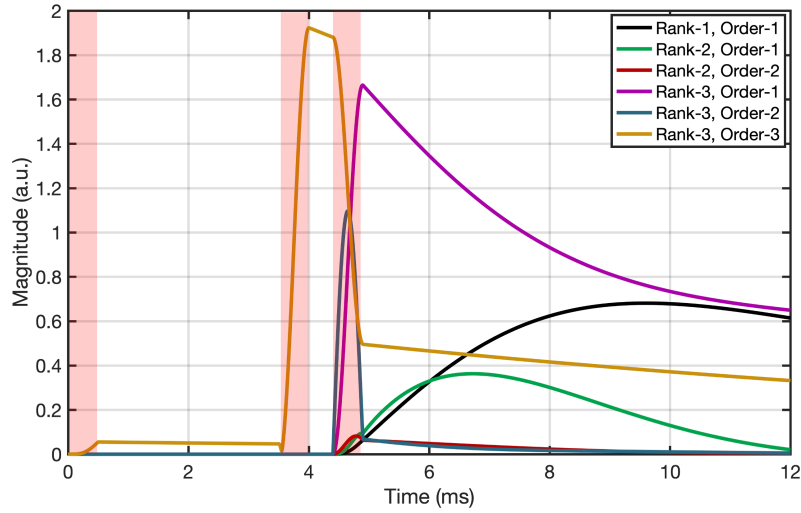


Figure 7: The summed coherences of the phase cycling steps. The red bars indicate periods of RF excitation. (color should be used for this figure in print)

5. Discussion

Based on the ISTO formalism for convenient description of spin-3/2 dynamics, we have demonstrated that the Redfield equation can be simplified for the case of ^{23}Na in biological tissue, leading to a generalised description of the ^{23}Na spin system; the SBE captures the combined effect of the residual Zeeman field, the RF field, and the static and fluctuating components of EFG.

The highly accessible form of the SBE system matrix, \mathbf{L} , provides a structured and intuitive representation of sodium dynamics for the sodium imaging research community, and will likely enable advances in ^{23}Na pulse and pulse sequence design. There is no need for a piecewise treatment to analyse a sequence, and thus simulation is made trivial: the definition of a 15x15 matrix of a known parameterised form (see Fig. 1), and a one-line call to an ode solver. Moreover, the SBE can be used to model echo formation, either by computation over a number of isochromats or integrating extended phase graph theory [18]. Our formalism may find application in the description of other spin-3/2 systems, and for ^{23}Na in NMR experiments in which the motion of the environment is sufficiently larger than the RF nutation and quadrupolar coupling.

We verified the behaviour of the Sodium Bloch equation through simulations, demonstrating the expected negligible difference between it and the spin-1/2 Bloch equation for fluid regions. However, for biological tissue environments, the deviations between sodium and proton dynamics are more pronounced, and depend on the specifics of the pulse sequence. It is therefore necessary to understand the form of the spin system and have an easy path to simulation to enable depth of understanding.

The Sodium Bloch equation will be a crucial tool in accurate Magnetic Resonance Fingerprinting (MRF) approaches to sodium imaging. Recently, Kratzer et al. [12] assumed that the proton Bloch equation was a sufficient first-order approximation of sodium dynamics to build the MRF dictionary. A hard pulse approximation was used in simulations, with results suggesting errors below 6.4% for brain tissue. For more extreme parameter sets, such as cartilage, the authors suggested further investigations. The Sodium Bloch equation's 15x15 system matrix can be substituted in place of the Bloch equation 3x3 matrix, removing need for approximation and reducing the error to zero.

6. Conclusion

In this work, we have presented the SBE as a generalised representation of ^{23}Na spin dynamics in biological tissue environments. To demonstrate the applicability of the formalism, we have analysed three types of ^{23}Na MRI pulse sequences in a range of biological environments. In addition, we have demonstrated the approximations and discrepancies when the spin-1/2 Bloch equation is employed in place of its 15-dimensional counterpart proposed here-in.

Appendix A Derivation of the matrix form of R

Consider the spectral density, $J(\omega)$ [5],

$$\begin{aligned} J(\omega) &= \frac{(2\pi)^2}{20} \frac{\chi^2 \tau_c}{1 + (\omega \tau_c)^2} \\ &\approx \int_0^\infty \left(\frac{eQ}{\hbar} \right)^2 \langle [F_{2m}^*(t) - \langle F_{2m}^* \rangle] [F_{2m}(t - \tau) - \langle F_{2m} \rangle] \rangle e^{i\omega\tau} d\tau, \end{aligned} \tag{A.13}$$

where χ is the quadrupolar coupling constant and τ_c is the correlation time.

The term $e^{-i\hat{H}_D\tau}\hat{T}_{2m}^\dagger e^{i\hat{H}_D\tau}$ in Eq.9 represents the evolution of \hat{T}_{2m}^\dagger under the influence of \hat{H}_D . Thus, its dynamic equation is

$$\frac{d}{dt}\mathbf{T} = \mathbf{DT}. \quad (\text{A.14})$$

The term $e^{-i\hat{H}_D\tau}\hat{T}_{2m}^\dagger e^{i\hat{H}_D\tau}$ is equivalent to the integral of Eq.A.14 over $[0, \tau]$ with the initial condition $\mathbf{T}(0) = \hat{T}_{2m}^\dagger$. Note that \mathbf{D} is skew-Hermitian. Therefore, it is diagonalisable and the eigenvalues are purely imaginary. Eq.A.14 can be rewritten as

$$\frac{d}{dt}\mathbf{T} = \mathbf{Q}^{-1} \begin{bmatrix} i\lambda_1 & & \\ & \ddots & \\ & & i\lambda_{15} \end{bmatrix} \mathbf{QT}, \quad (\text{A.15})$$

where λ_k 's are the eigenvalues and \mathbf{Q} is the eigenvector matrix. By defining $[q_{1,s}, \dots, q_{15,s}]^\top$ as the s -th column in \mathbf{Q} corresponding to the initial condition such that $\mathbf{T}_s = \hat{T}_{2m}$, we obtain the expression of $e^{-i\hat{H}_D\tau}\hat{T}_{2m}^\dagger e^{i\hat{H}_D\tau}$ in the ISTO basis,

$$\begin{aligned} e^{-i\hat{H}_D\tau}\hat{T}_{2m}^\dagger e^{i\hat{H}_D\tau} &= \mathbf{Q}^{-1} \begin{bmatrix} (-1)^m q_{1,s} e^{i\lambda_1 \tau} \\ \vdots \\ (-1)^m q_{15,s} e^{i\lambda_{15} \tau} \end{bmatrix} \\ &= \frac{1}{\det(\mathbf{Q})} \begin{bmatrix} Q_{1,1} & \dots & Q_{15,1} \\ \vdots & \ddots & \vdots \\ Q_{1,15} & \dots & Q_{15,15} \end{bmatrix} \begin{bmatrix} (-1)^m q_{1,s} e^{i\lambda_1 \tau} \\ \vdots \\ (-1)^m q_{15,s} e^{i\lambda_{15} \tau} \end{bmatrix} \\ &= \frac{1}{\det(\mathbf{Q})} \begin{bmatrix} (-1)^m \sum_k Q_{k,1} q_{k,s} e^{i\lambda_k \tau} \\ \vdots \\ (-1)^m \sum_k Q_{k,15} q_{k,s} e^{i\lambda_k \tau} \end{bmatrix} \\ &= \sum_{l=1}^3 \sum_{n=-l}^l \sum_{k=1}^{15} \alpha_{klmn} e^{i\lambda_k \tau} \hat{T}_{ln}, \end{aligned} \quad (\text{A.16})$$

where α_{klmn} is introduced to denote the coefficient.

Rearrange and simplify Eq.9 by the following steps:

$$\begin{aligned} \hat{\Gamma}(\hat{\rho}) &= - \sum_{m=-2}^2 \left[\hat{T}_{2m}, \left[\sum_{l,n} \sum_k \alpha_{klmn} J(m\omega_r + \lambda_k) \hat{T}_{ln}, \hat{\rho} \right] \right] \\ &\approx - \sum_{m=-2}^2 \left[\hat{T}_{2m}, \left[\sum_{l,n} \sum_k \alpha_{klmn} J(m\omega_0) \hat{T}_{ln}, \hat{\rho} \right] \right] \\ &= - \sum_{m=-2}^2 \left[\hat{T}_{2m}, \left[\sum_{l,n} \sum_k \alpha_{klmn} \hat{T}_{ln}, \hat{\rho} \right] \right] J(m\omega_r) \\ &= - \sum_{m=-2}^2 \left[\hat{T}_{2m}, \left[\hat{T}_{2m}^\dagger, \hat{\rho} \right] \right] J(m\omega_0) \end{aligned} \quad (\text{A.17})$$

Here, there are two key steps in the derivation. Firstly, the eigenvalues are upper-bounded according to Bendixson's inequality [19]

$$\lambda \leq 15 \max(|d_{ij}|) \quad (\text{A.18})$$

where d_{ij} are the elements of \mathbf{D} and in the same order of magnitude as ω_1 , ω_Δ and ω_Q . Since $\lambda \ll 1/\tau_c$ in biological environments and $\omega_r \approx \omega_0$, we have $J(m\omega_r + \lambda_k) \approx J(m\omega_0)$. Conventionally, $J(m\omega_0)$ is also denoted as J_m .

Secondly, summing the products of elements and cofactors results in [20]

$$\sum_k \alpha_{klmn} = \begin{cases} (-1)^m & \text{when } l = 2 \text{ and } n = m \\ 0 & \text{otherwise} \end{cases} \quad (\text{A.19})$$

Eq.A.17 suggests that the effect of \hat{H}_D is negligible in the relaxation process because the interaction occurs on a slow timescale, and can therefore be approximated by the case $\hat{H}_D = 0$. The expression of \mathbf{R} follows from expansion of the double commutator [5].

References

- [1] G. Madelin, R. Kline, R. Walwick, R. R. Regatte, A method for estimating intracellular sodium concentration and extracellular volume fraction in brain in vivo using sodium magnetic resonance imaging, *Scientific Reports* 4 (2014) 4763. doi:10.1038/srep04763.
- [2] G. Madelin, R. R. Regatte, Biomedical applications of sodium MRI in vivo, *Journal of Magnetic Resonance Imaging* 38 (3) (2013) 511–529. doi:10.1002/jmri.24168.
- [3] R. Ouwerkerk, R. H. Morgan, ^{23}Na MRI: From Research to Clinical Use, *J Am Coll Radiol* 4 (10) (2007) 739–741.
- [4] G. J. Bowden, W. D. Hutchison, Tensor Operator Formalism for Multiple-Quantum NMR: 1. Spin-1 Nuclei, *Journal of Magnetc Resonance* 67 (1986) 415–437.
- [5] J. R. van der Maarel, Thermal relaxation and coherence dynamics of spin 3/2. I. Static and fluctuating quadrupolar interactions in the multipole basis, *Concepts in Magnetic Resonance* 19A (2) (2003) 97–116. doi:10.1002/cmr.a.10087.
- [6] R. Kharrazian, P. M. Jakob, Dynamics of ^{23}Na during completely balanced steady-state free precession, *Journal of Magnetic Resonance* 179 (1) (2006) 73–84. doi:10.1016/j.jmr.2005.11.008.
- [7] C. Tanase, F. E. Boada, Algebraic description of spin 3/2 dynamics in nmr experiments, *Journal of Magnetic Resonance* 173 (2) (2005) 236–253.
- [8] I. Hancu, J. R. C. van der Maarel, F. E. Boada, A Model for the Dynamics of Spins 3/2 in Biological Media: Signal Loss during Radiofrequency Excitation in Triple-Quantum-Filtered Sodium MRI, *Journal of Magnetic Resonance* 147 (2) (2000) 179–191. doi:10.1006/jmre.2000.2177.
- [9] J. R. van der Maarel, Thermal relaxation and coherence dynamics of spin 3/2. II. Strong radio-frequency field, *Concepts in Magnetic Resonance* 19A (2) (2003) 117–133. doi:10.1002/cmr.a.10088.
- [10] R. Stobbe, C. Beaulieu, In vivo sodium magnetic resonance imaging of the human brain using soft inversion recovery fluid attenuation, *Magnetic Resonance in Medicine* 54 (5) (2005) 1305–1310. doi:10.1002/mrm.20696.
- [11] G. Madelin, J.-S. Lee, S. Inati, A. Jerschow, R. R. Regatte, Sodium inversion recovery MRI of the knee joint in vivo at 7T, *Journal of Magnetic Resonance* 207 (1) (2010) 42–52. doi:10.1016/j.jmr.2010.08.003.
- [12] F. J. Kratzer, S. Flassbeck, A. M. Nagel, N. G. Behl, B. R. Knowles, P. Bachert, M. E. Ladd, S. Schmitter, Sodium relaxometry using ^{23}Na MR fingerprinting: A proof of concept, *Magnetic Resonance in Medicine* 84 (5) (2020) 2577–2591.
- [13] J.-S. Lee, R. R. Regatte, A. Jerschow, Optimal excitation of ^{23}Na nuclear spins in the presence of residual quadrupolar coupling and quadrupolar relaxation, *The Journal of Chemical Physics* 131 (17) (2009) 174501. doi:10.1063/1.3253970.

- [14] B. E. Chapman, C. Naumann, D. J. Philp, U. Eliav, G. Navon, P. W. Kuchel, z-spectra of $^{23}\text{Na}^+$ in stretched gels: Quantitative multiple quantum analysis, *Journal of Magnetic Resonance* 205 (2) (2010) 260–268.
- [15] G. J. Bowden, W. D. Hutchison, Tensor Operator Formalism for Multiple-Quantum NMR. 2. Spins 32, 2 and 52 and General I, *Journal of Magnetic Resonance* 67 (1986) 415–437.
- [16] T. Wilferth, L. V. Gast, R. W. Stobbe, C. Beaulieu, B. Hensel, M. Uder, A. M. Nagel, ^{23}Na MRI of human skeletal muscle using long inversion recovery pulses, *Magnetic Resonance Imaging* 63 (2019) 280–290. doi:10.1016/j.mri.2019.08.012.
- [17] I. Hancu, F. E. Boada, G. X. Shen, Three-dimensional triple-quantum-filtered ^{23}Na imaging of in vivo human brain, *Magnetic Resonance in Medicine* 42 (1999) 1146–54.
- [18] M. Weigel, Extended phase graphs: dephasing, rf pulses, and echoes-pure and simple, *Journal of Magnetic Resonance Imaging* 41 (2) (2015) 266–295.
- [19] I. Bendixson, et al., Sur les racines d'une équation fondamentale, *Acta Mathematica* 25 (1902) 359–365.
- [20] J. Liesen, V. Mehrmann, *Linear algebra*, Springer, 2015.